Appendix A

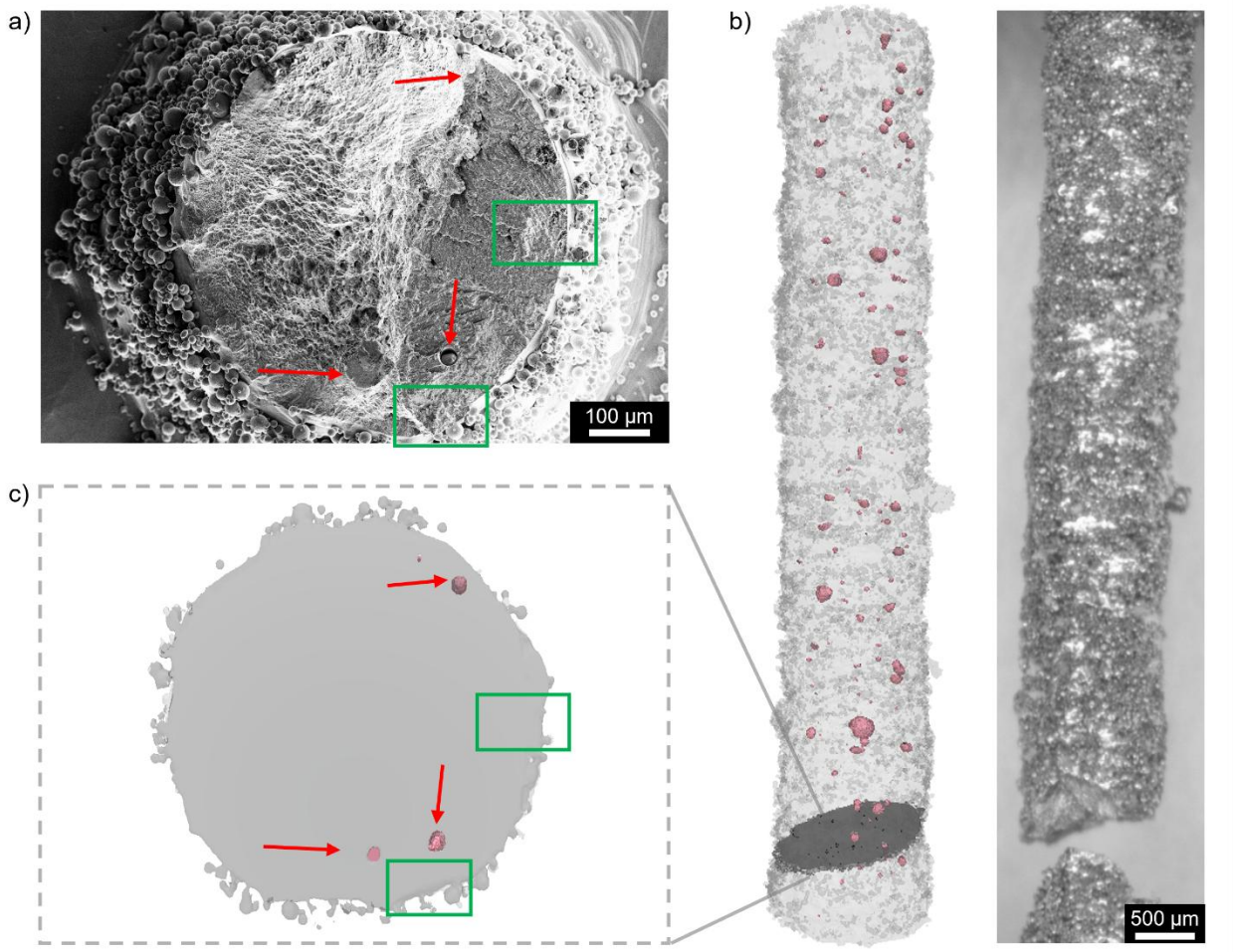

Figure S1 - Characterization of the fracture surface of the 90° strut. (a) SEM fracture surface. Scale bar set at 100 µm. (b) Axial failure location shown by stereomicroscopy (right) and corresponding CT-reconstructed strut (left). The latter shows in pink the CT-detected internal porosity. The scale bar for the stereomicroscopy image is set at 500 µm. (c) CT-derived cross-section extracted at the fracture plane, with internal porosity rendered in pink. Red arrows in (a) and (c) indicate subsurface pores, while green boxes highlight surface micro-notches associated with fatigue crack initiation.

Figure S1 provides a complementary visualization of the fracture site of the 90° struts discussed in *Section 2.4*. Figure S1a shows the same SEM fracture surface reported in Figure 4a at a larger field of view, enabling direct comparison with the CT-derived cross-section extracted at the same axial position along the gauge length (Figure S1c). In Figure S1c, internal porosity resolved by CT scanning prior to fatigue testing is shown in pink. Red arrows in Figures S1a and S1c identify subsurface pores exposed at the fracture plane, whereas green boxes highlight surface micro-notches associated with fatigue crack initiation.

Figure S1b locates the failure location within the strut's gauge length. The stereomicroscopy image (right) shows the fracture position on the tested specimen, while the corresponding CT-reconstructed 90° strut is shown on the left, with the surface rendered transparent to visualize the internal porosity distribution and the fracture zone (darker grey).

Appendix B

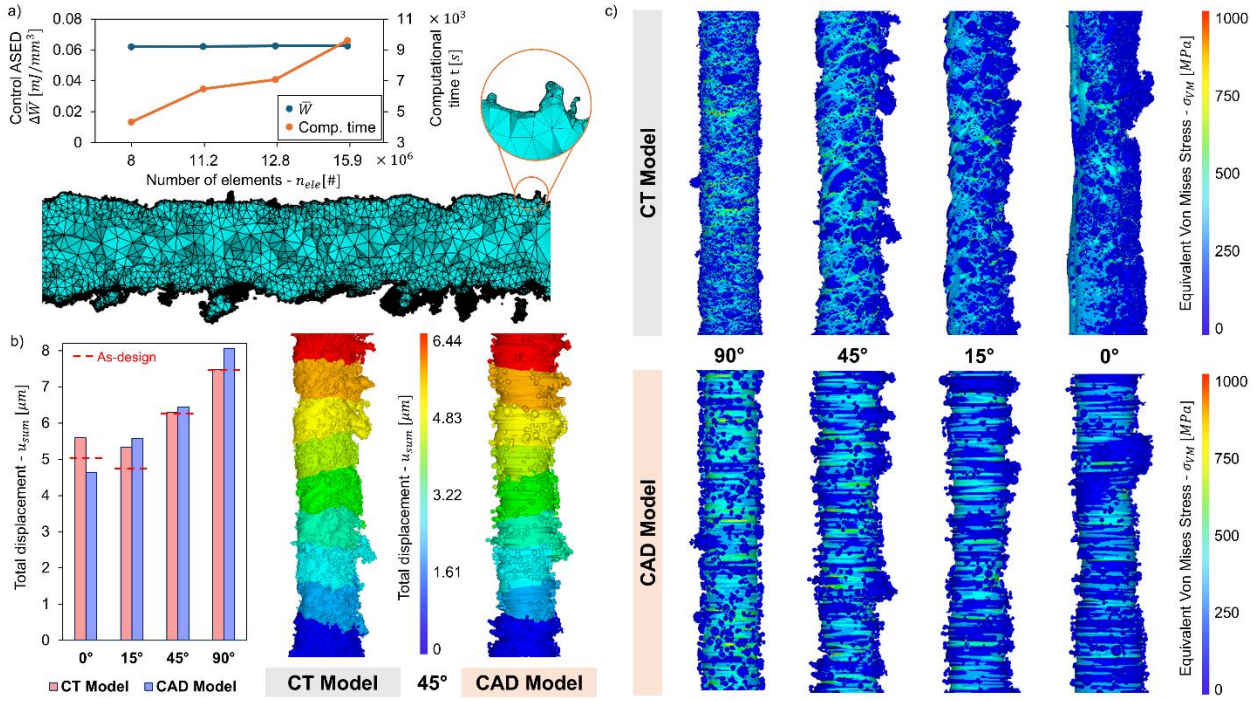

Figure S2: a) Mesh convergence example for the finite element simulation of thin strut reconstructed geometries. b) Comparison of the displacement fields and the maximum displacements between micro-CT reconstructed geometries and synthetic CAD models. c) Direct comparison between the equivalent Von Mises stress distribution for micro-CT reconstructed geometries and synthetic CAD models.

Figure S2a depicts the mesh convergence study and the resulting finite element mesh obtained for the CT-based geometry reconstructions and for the synthetic as-built CAD geometries. In both cases, the meshing parameters are provided after a convergence case study, where displacements, computational time and a control point for Average Strain Energy Density (ASED) calculation are considered. The reconstructed geometry of the 45° specimen is selected as representative case study for the entire simulation set and different finite element models characterized by variable mesh parameters are conducted. The meshing process is conducted using the nTop v5.36.2 (nTopology, USA) software. The mesh is highly refined on the specimen surface to improve the precision on the local defects, and its dimension is kept constant with the same refinement degree over a given thickness to ensure stability in the ASED calculation. After this initial step, the mesh dimension is gradually increased moving radially toward the specimen axis to reduce the computational cost. In the convergence analysis the influence of the parameters for the mesh dimension is studied along with the influence of the decimation on the CT-reconstructed mesh geometry. The most important metric in this convergence analysis is the control ASED: one critical point is arbitrarily selected in the geometry and the ASED computations are performed. Results, displayed in Figure S2a, show consistency in the control ASED calculations even for a reduced number of elements which is directly linked to a more efficient computation. The optimal parameter configuration is the one minimizing the computational time and it is presented in Figure

S2a; the associated mesh parameters are listed in Table S1. Finite element linear elastic simulations are performed in ANSYS Mechanical APDL v2024R1 (ANSYS, USA) with quadratic solid elements SOLID187.

Table S1 - Mesh parameters for optimal simulation performances

Mesh parameters	
Decimation	80%
Surface mesh dimension	0.05 mm
Constant mesh thickness	0.1 mm
Inner mesh inflation rate	20

Figure S2b depicts the deformations associated with each CT-synthetic CAD couple. It can be noticed a substantial agreement between the two models, with the synthetic CAD more compliant with respect to the CT geometrical reconstruction in 15°, 45°, and 90° configurations. This behaviour is linked to the different representation of the parasitic masses between the synthetic CAD and the CT geometry: this contribution is lightly underestimated in the CAD reconstruction. An opposite trend is registered instead for the 0° configuration, where the parasitic masses identified on the lowerskin of the strut are assimilated to a bulk cross-section by the synthetic CAD, generating a stiffer model with respect to the CT-based one. The effect of the parasitic masses in the as-built geometries can be also observed comparing the displacement results of both as-built models with the ones obtained in the as-designed configuration. The 45° and 90° configurations are characterized by a larger adherence between the as designed and the CT simulations, and this can be rooted to the more favourable printing orientation of these struts [1]. The 15° and 0°, in contrast, show a larger deviation, symptomatic of a larger geometrical discrepancy between the as-built and as-designed geometries.

Figure S2c depicts the equivalent Von Mises stress distribution of the CT reconstructed models and the synthetic CAD ones. While a global coherence is found among the different models, specific patterns are visible. In the synthetic CAD models, the ridges characteristic of the generation, act as stress raiser giving to the specimen a peculiar stress pattern orthogonal to the specimen axis. CT-based geometries instead are characterized by a stress distribution deriving from the specimen waviness, with specific inclination rooted in the specimen manufacturing process.